

Atomic Layer Deposition and Annealing of Co_3O_4 for Electrocatalytic Oxygen Evolution

Tejas Nivarty

Submitted under the supervision of Professor C. Daniel Frisbie to the University Honors Program at the University of Minnesota-Twin Cities in partial fulfillment of the requirements for the degree of Bachelor of Chemical Engineering, *summa cum laude* in Chemical Engineering.

April 21, 2022

I would like to thank Prof. Frisbie and Prof. Dauenhauer for trusting me with the keys to their labs, and Prof. Jalan for taking the time to be part of my committee. I would like to thank Amber Walton for her incredible mentorship and support in the writing of this thesis and all of the experiments performed herein. I would also like to thank Dr. Bruce Rayner of the Kurt J. Lesker Company for his assistance in troubleshooting the ALD process. Portions of this work were conducted both in the Minnesota Nano Center, which is supported by the National Science Foundation through the National Nanotechnology Coordinated Infrastructure (NNCI) under Award Number ECCS-2025124, and in the Characterization Facility, University of Minnesota, which receives partial support from the NSF through the MRSEC (Award Number DMR-2011401) and the NNCI (Award Number ECCS-2025124) programs.

1 Abstract

In the fight against climate change, renewable energy must be employed to reduce fossil fuel dependence. However, intermittent renewable energy sources like wind and solar require grid energy storage to be feasible at a large scale. Hydrogen shows promise as an energy storage medium, and is also an important chemical feedstock. However, current production of hydrogen is carbon-intensive, and green hydrogen produced by water electrolysis is expensive due to a lack of highly effective, non-precious metal oxygen evolution (OER) electrocatalysts. Co_3O_4 is one of the most effective metal oxide OER electrocatalysts, but thin films of Co_3O_4 produced via atomic layer deposition (ALD) have never been explored for OER.

Uniform thin films of Co_3O_4 were successfully produced via ALD using CoCp_2 and O_3 precursors, and the crystallinity and stoichiometry of these thin films were studied before and after annealing using X-ray photoelectron spectroscopy and X-ray diffraction. The catalytic decomposition of O_3 by Co_3O_4 during ALD was mitigated by using a 200 °C deposition temperature and a 10 s long O_3 pulse at 10 torr. 7 nm and 27 nm thick films showed no difference in surface stoichiometry after being deposited by ALD. Annealing under H_2 reduced Co_3O_4 films to CoO , as did annealing under N_2 at a high temperature. 27 nm Co_3O_4 films were found to be much more crystalline than 7 nm Co_3O_4 films before annealing, and 27 nm films showed improvements in crystallinity after annealing while 7 nm films did not.

Contents

1	Abstract	1
2	Motivation	3
3	Background	4
3.1	Water Electrolysis	4
3.2	Cobalt Oxide as an OER Catalyst	6
3.3	Atomic Layer Deposition (ALD)	7
4	ALD Process Optimization	9
4.1	Methods and Materials	9
4.2	Optimization	11
5	Annealing and Characterization	16
5.1	Experimental Methods	16
5.2	Results	17
6	Conclusions	20
7	Future Work	20
8	References	21

2 Motivation

Climate change is the rapid shift in global climate patterns primarily caused by greenhouse gases such as CO_2 , CH_4 , and N_2O .¹ Climate change has been linked to decreased agricultural output,² increases in the number of wildfires,³ and loss of biodiversity.⁴ Climate change and its negative impacts are fueled by the burning of fossil fuels, chiefly oil, natural gas, and coal. In 2020, over 83% of total global energy use came from fossil fuels.⁵

Although the proportion of global energy from renewable sources like solar energy, wind energy, and hydroelectric energy continue to grow, they present key issues limiting their growth. Hydroelectric energy generation is geographically limited to areas with major rivers, and has been found to cause ecological damage where installed.⁶ Solar and wind energy are intermittent energy sources that necessitate grid energy storage to be feasible.^{7,8} While the geography of major rivers cannot change, fundamentally limiting the expansion of hydroelectric power generation, better grid energy storage technology is paramount to successfully implementing geographically untethered renewable energy sources.

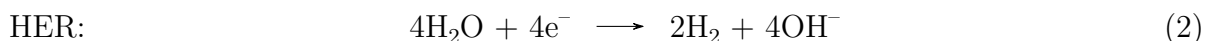
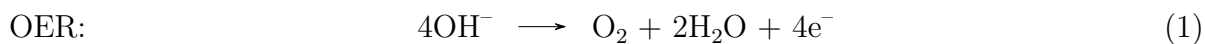
Numerous ideas for grid energy storage have been proposed, including pumped hydro storage, redox flow batteries, hydrogen fuel cells, and supercapacitors.⁹ Hydrogen as an energy storage medium is advantageous due to its high specific energy. Apart from its potential for grid energy storage, hydrogen is also an essential chemical feedstock. Along with N_2 , it is the primary feedstock for the Haber-Bosch process that generates 150 million tons of ammonia per year, 85% of which is used in the production of fertilizers.¹⁰

The current production of hydrogen is associated with significant carbon emissions, as 95% of hydrogen is produced from fossil fuels.¹¹ Water electrolysis using intermittent renewable energy sources shows promise to decarbonize hydrogen production and create "green hydrogen", but is currently underutilized due to the high capital and operating costs of current precious metal electrocatalysts. Therefore, cheaper and more effective electrocatalysts are needed to create a green hydrogen economy.

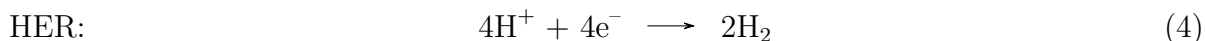
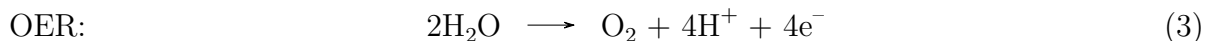
3 Background

3.1 Water Electrolysis

Water electrolysis is an electrolytic reaction where oxygen evolution (OER) and hydrogen evolution (HER) occur on a positively charged anode and a negatively charged cathode, respectively. Under alkaline conditions, the reactions are:¹²



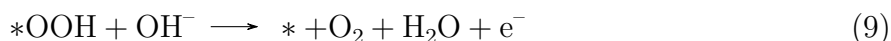
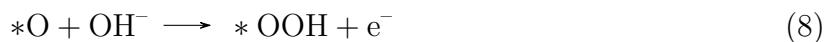
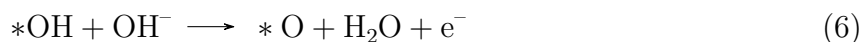
And under acidic conditions:¹²



The thermodynamic potential required to drive OER is 1.23 V vs. the reversible hydrogen electrode (RHE).¹³ However, a much higher potential is required to drive the reaction practically. The potential in excess of the thermodynamic potential is called the overpotential. While electrocatalysts that decrease overpotentials for both HER and OER have been studied, low overpotential, non-precious metal HER catalysts have been discovered,¹⁴ while even the best non-precious metal OER catalysts suffer from large overpotentials.¹⁵

HER is generally accepted to have two distinct electron transfer steps, while OER has four. There are two proposed mechanisms of OER under alkaline conditions:¹⁶ both mechanisms begin with a hydroxide anion adsorbing onto an active site (reaction five) and subsequently being oxidized by another hydroxide anion to yield O* (reaction six). However, the resulting O* species could either react with a neighboring O* species to form O₂ (reaction

seven) or react with another OH^- species to form a $^*\text{OOH}$ peroxide intermediate (reaction eight) which then reacts with another OH^- species to form O_2 (reaction nine). The acidic OER mechanism was not considered in this project, as metal oxides, the highest performing OER catalysts, are more prone to degradation in acidic media as compared to alkaline media.¹⁵



The free energies of the intermediates $^*\text{O}$, $^*\text{OH}$, and $^*\text{OOH}$ scale in a consistent way across many different catalytic surfaces. Both $\Delta G_{^*\text{OOH}} = \Delta G_{^*\text{OH}} + 3.2 \pm 0.2 \text{ eV}$ and $\Delta G_{^*\text{O}} = 2\Delta G_{^*\text{OH}} + 0.4 \text{ eV}$ are consistently observed over many different catalytic surfaces.¹⁷ The scaling relationship between $^*\text{OOH}$ and $^*\text{OH}$ is the main cause of the high overpotentials observed in OER catalysts. This is because the overall energy change between H_2O and O_2 is 4.92 eV, meaning that for any one electron transfer step, the most even (and therefore optimal) energy change

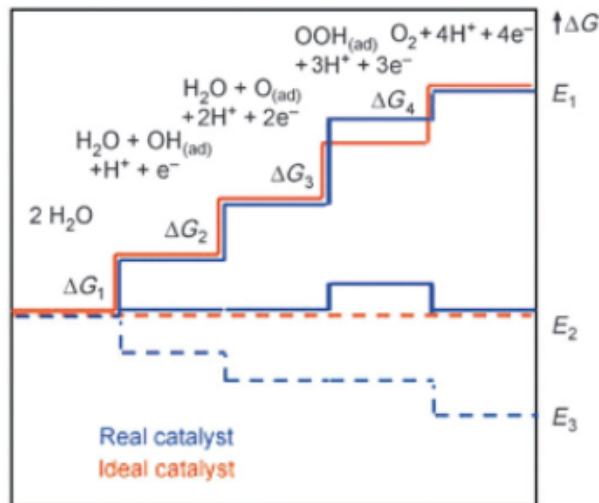


Figure 1: Gibbs free energy level diagram of the OER mechanism.¹² A real catalyst with the scaling relationship is shown in blue, while an ideal catalyst without a scaling relationship is shown in red. $E_1 = 0 \text{ V}$, $E_2 = 1.23 \text{ V}$, and $E_3 - E_2$ represents the overpotential required to drive OER with current electrocatalysts.

is $\frac{4.92 \text{ eV}}{4} = 1.23 \text{ eV}$. This is illustrated in

Figure 1. For the two electron transfers that take place between *OOH and *OH, this means the optimal scaling relationship is $1.23 \text{ eV} \times 2 = 2.46 \text{ eV}$. With this, the minimum overpotential caused by the scaling relationship between *OOH and *OH can be calculated:¹⁸

$$\frac{(3.2 \pm 0.2 \text{ eV}) - 2.46 \text{ eV}}{2 e} = 0.4 \pm 0.1 \text{ V} \tag{10}$$

Figure 2 shows overpotential data taken from many metal oxide electrocatalysts plotted against the difference in the free energies of adsorbed *O and *OH species in said electrocatalyst. The data fits the general trend of a Sabatier volcano, showcasing the accuracy of the descriptor. Additionally, it shows that the best electrocatalysts have an overpotential of roughly 0.4 V as predicted by Equation 10.

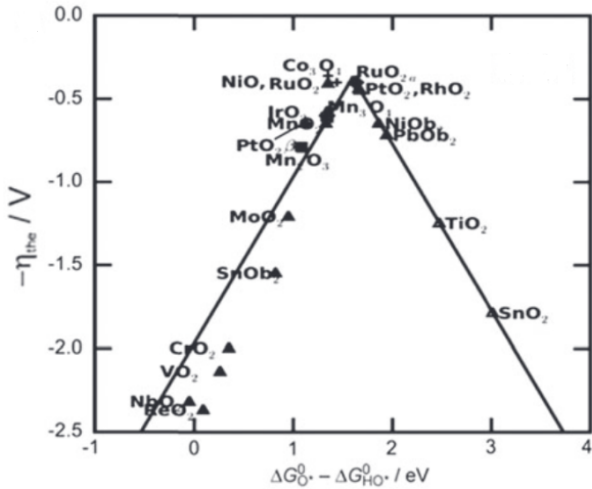


Figure 2: Sabatier volcano diagram of metal oxide OER catalysts.¹²

3.2 Cobalt Oxide as an OER Catalyst

Near the peak of the volcano plot in Figure 2 is spinel Co_3O_4 , which has been extensively studied as an OER electrocatalyst.¹⁹⁻²¹ It has a moderate oxygen binding affinity, placing it at the Sabatier optimal. The two most thermodynamically stable forms of cobalt oxide are Co_3O_4 , which contains one Co^{+2} cation for every Co^{+3} cation, and CoO , which only contains Co^{+2} cations.²² Co_3O_4 is a p-type semiconductor at room temperature with a band gap of 1.6 eV.²³

There has been debate about the active sites for OER in Co_3O_4 . Wang et. al.²⁴ sub-

stituted Zn^{+2} and Al^{+3} cations for Co^{+2} and Co^{+3} cations, respectively, and concluded that Co^{+2} is the primary active site for OER. However, Liu et. al.¹⁹ analyzed OER performance on different crystal facets of Co_3O_4 , each with their own proportion of Co^{+2} to Co^{+3} cations and determined that Co^{+3} ions exhibit higher activity for OER. Recent density functional theory (DFT) calculations agree and suggest that Co^{+3} is the primary active site for OER.²⁵ Surface oxygen vacancies in Co_3O_4 also play a significant role in OER activity.²⁶ Oxygen vacancies free up electrons in the lattice, pushing them into the band gap. This leads to an overall increase in the conductivity of Co_3O_4 , increasing its OER activity.

There have been a number of techniques employed to decrease the overpotential of OER using Co_3O_4 :²⁷ creating Co_3O_4 with different morphologies,²⁸ doping Co_3O_4 with different heteroatoms,²⁹ and creating Co_3O_4 composites with other materials.³⁰ However, conformal thin films of Co_3O_4 have never been explored for the oxygen evolution reaction.

3.3 Atomic Layer Deposition (ALD)

Atomic layer deposition (ALD) is a thin film deposition technique that has excellent conformity to substrate surfaces. A subset of chemical vapor deposition (CVD), it utilizes sequential pulses of gas-phase precursors under vacuum to achieve a self-limiting surface reaction on a substrate.

The most common type of ALD process is an A-B process (see Figure 3), which occurs in four repeating steps. In step one, reactant A is flooded into the reactor and saturates all of the reactive surface sites on the substrate. In step two, the reactor is purged of excess reactant A and reaction byproducts by flowing an inert carrier gas through the reactor. In step three, reactant B is flooded into the reactor and reacts with the reactive surface sites left by reactant A. In step four, excess reactant B and reaction byproducts are purged from the reactor. Step one can then be repeated, as the same reactive surface sites exist on the newly grown layer. To synthesize metal oxide thin films via ALD, reactant A is typically a pyrophoric organometallic compound, and reactant B is an oxidizing agent such as H_2O , O_2 ,

or O_3 . The vigorous reaction between pyrophoric compounds and oxidizing agents means that less reactant/precursor can be used to carry out the reaction, making the ALD process more efficient.

Co_3O_4 has been grown via ALD using many different precursors, including $Co(thd)_2$ and O_3 ,³² dicobalt hexacarbonyl t-butylacetylene (CCTBA) and O_3 ,³³ and $CoCp_2$ and O_3 .³⁴ Of these precursors, $CoCp_2$ has the advantages of being widely commercially available, able to deposit within a moderate ALD temperature window from 175 to 275 °C, and able to deposit on the widely available $\langle 100 \rangle Si$ substrate, both on thermally grown SiO_2 and native SiO_2 .

The two most important parameters to note when optimizing ALD processes are growth per cycle (GPC) and uniformity. GPC is the thickness by which an ALD film grows upon each ALD cycle, and it can be used to judge the quality of an ALD film. For example, a higher GPC than expected could indicate the presence of parasitic chemical vapor deposition (CVD), where product is being formed in the gas phase and depositing onto the substrate rather than a surface reaction occurring, necessitating less reactant be used or purge times be lengthened. Uniformity is the evenness of the deposited thin film, which is desirable to ensure that film thickness can be easily controlled. There are many potential causes of non-uniformity: overlapping precursor pulses leading to parasitic CVD, thermal decomposition of precursors, non-uniform gas distribution in the reactor, and parasitic side reactions.³⁵ Non-uniformity can be calculated by using Equation 11, where σ is the standard deviation of thickness measurements and μ is the average thickness measure-

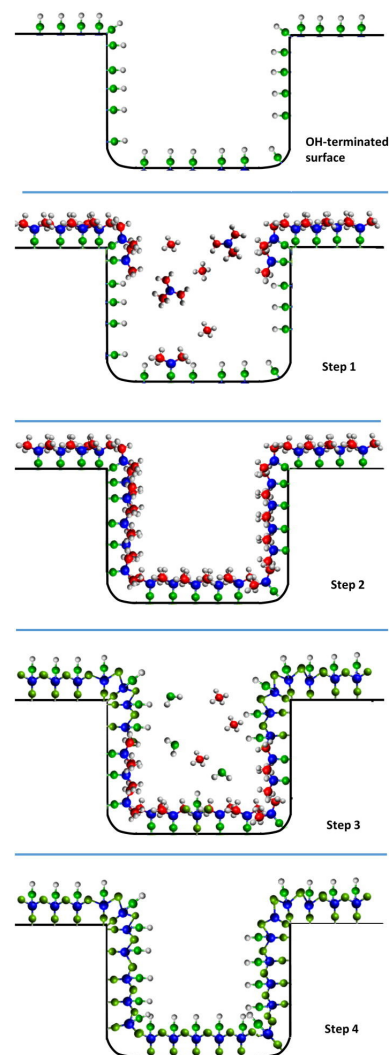


Figure 3: Outline of an A-B ALD process: Al_2O_3 deposition from $Al(CH_3)_3$ and H_2O .³¹

ment.

$$\text{Non-uniformity}\% = \frac{\sigma}{\mu} \quad (11)$$

Another important constraint when designing an ALD process is the ALD window (see Figure 4). Much like optimizing other ALD parameters, this window is typically characterized by a region of deposition temperatures in which GPC is stable.

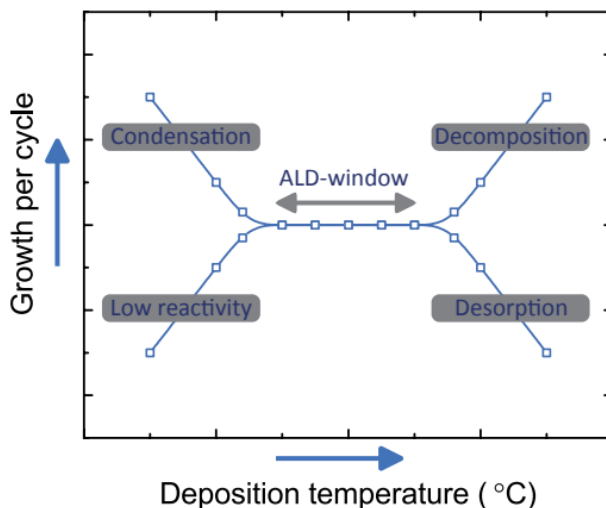


Figure 4: Diagram of a typical ALD temperature window showing the effects of temperature on growth per cycle (GPC).³⁶ Either of the four phenomena described could occur depending on the specific ALD chemistry used.

4 ALD Process Optimization

4.1 Methods and Materials

The Co_3O_4 ALD process was initially based off of the work of Holden and Conley,³⁴ who had grown Co_3O_4 from CoCp_2 and O_3 on $\langle 100 \rangle \text{Si}/\text{SiO}_2$ substrates. They investigated both thermally grown SiO_2 and native SiO_2 substrates and found GPCs of 0.043 and $0.5 \frac{\text{nm}}{\text{cycle}}$, respectively. They also discovered that the ALD window lies between 175 °C and 275 °C. They deposited Co_3O_4 at 250 °C and achieved a non-uniformity of 4.7% over a 5 in wafer.

To deposit the films, a Kurt J. Lesker (KJL) ALD-150LE system was used. The system had two separate lines to deliver precursor gas to the reactor where the substrate was located. One line was connected to a precursor manifold with interchangeable precursors, and the other was connected to an O_3 generator. Both lines had N_2 flow available as a carrier and purge gas. To evenly distribute the precursor gas over the substrate, the KJL ALD system had a showerhead pattern at the entrance of the reactor.

A $CoCp_2$ precursor ampoule purchased from Strem was connected to the system and heated to $100\text{ }^\circ\text{C}$ to ensure sufficient volatility. O_3 was generated within the ALD system by feeding O_2 into an ozone generator. The process variables considered were the pulse times of the $CoCp_2$ and O_3 , the N_2 purge time and flowrate, the substrate heater temperature, the pressure of the incoming O_3 , and the precursor valve and delivery line temperatures. To measure film thickness, variable-angle spectroscopic ellipsometry (VASE) was used. The VASE fitting model for Co_3O_4 was based off of data taken by Holden and Conley.³⁴ All films in this study were grown on native SiO_2 substrates. The thickness of the native SiO_2 layer on the substrate was measured before ALD using the FilmSense native SiO_2 model, and these measurements were used to fit the Co_3O_4/SiO_2 VASE model after ALD.

The general approach for ALD optimization was to grow films at 336 cycles, which should yield an expected film thickness of 16.80 nm from the $0.5\text{ }\frac{nm}{cycle}$ measured by Holden and Conley. Then, based off of the thickness measurements, ALD process parameters were changed to achieve a uniform film with a consistent GPC. Process parameters were always changed based off of the settings of the previous ALD run.

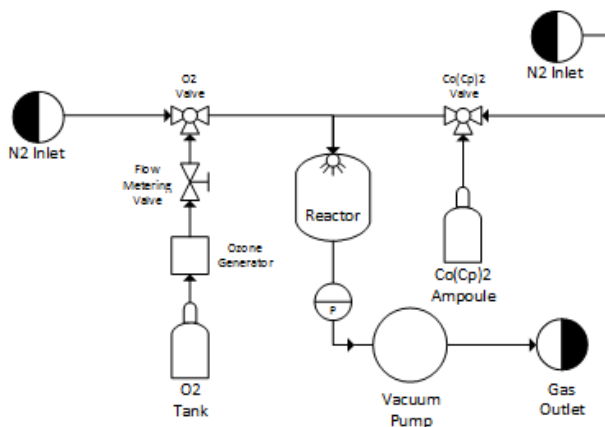
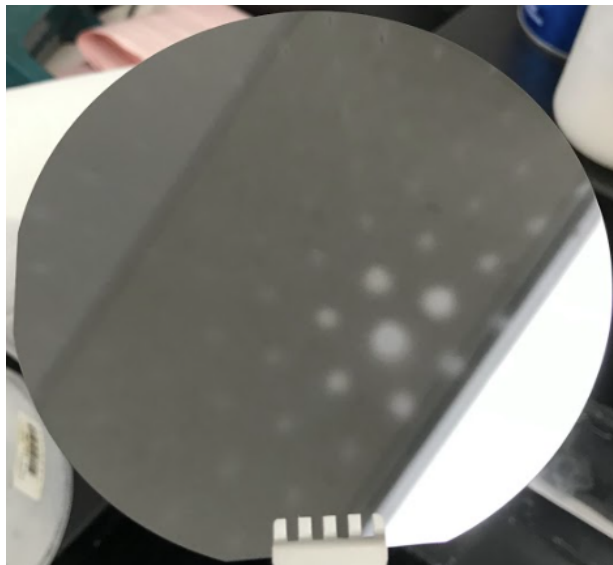


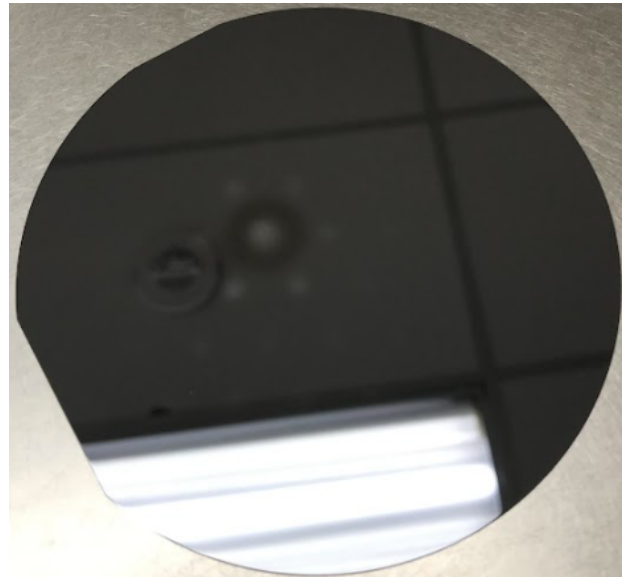
Figure 5: A simplified process flow diagram of the KJL ALD system. The temperatures of the $CoCp_2$ ampoule, $CoCp_2$ valve, the $CoCp_2$ delivery line, and the reactor can all be controlled independently.

4.2 Optimization

The first film grown in the KJL ALD system (Figure 6a) displayed uneven deposition. The pattern of the showerhead became visible on the substrate. Within the spots, a maximum thickness of 10.76 nm was measured, while the thickness outside of these spots was measured to be 1.04 nm. Because the observed film thicknesses were lower than the expected 16.80 nm, a lack of precursor was suspected to be the cause of the spotting.



(a) Image of the first ALD film grown on the KJL ALD system, with a 0.3 s CoCp_2 pulse time and an O_3 pressure of 0.1 torr. The superimposed showerhead pattern (spotting) is clearly visible.



(b) Image of a Co_3O_4 thin film grown with a 1 s CoCp_2 pulse time and an O_3 pressure of 5 torr. A dark ring of Co_3O_4 33.58 nm thick is visible within the showerhead pattern.

Figure 6: Images of ALD films grown with 336 cycles of 10s/10s/10s ($\text{N}_2/\text{O}_3/\text{N}_2$), a N_2 flowrate of 50 sccm in both source lines, and with the substrate heater at 271 °C.

Therefore, for the next ALD film, the CoCp_2 pulse time was increased to 0.6 s. However, the same spotting pattern in Figure 6a and low overall growth was still observed. Because of this, the CoCp_2 pulse time was found to not be the limiting precursor, and the O_3 pulse time was instead increased to 15 s. Although spotting similar to Figure 6a was still observed, the film thickness measured in the spots increased to 4.97 nm from the 1.70 nm observed in the previous film. It was therefore concluded that the primary cause of non-uniformity was a

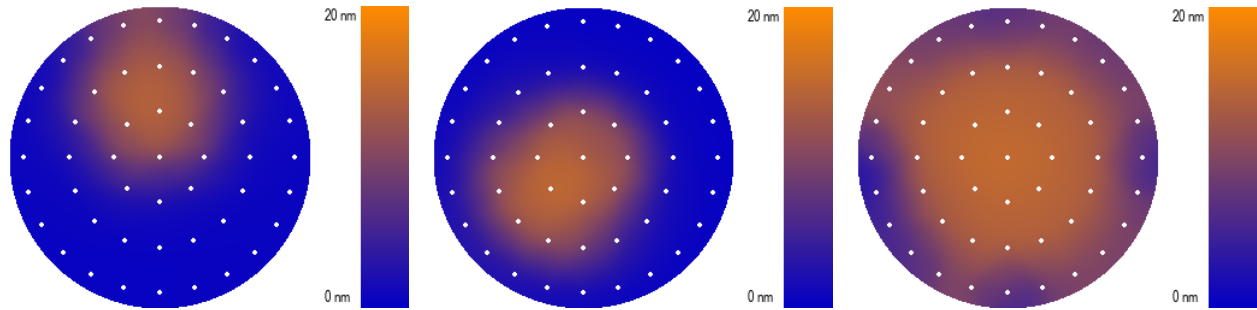
lack of O_3 in the reactor.

To deliver more O_3 to the reactor, O_3 pressure was instead increased to 2 torr and pulse time was decreased back to 10 s. The increase in O_3 pressure to 2 torr led to a dramatic increase in the maximum film thickness within the spots to 14.40 nm, much closer to the expected 16.8 nm. The thickness outside of the spots also increased to 6.73 nm. To rule out the possibility of the process now being limited by $CoCp_2$, its pulse time was increased to 1 s, which led to a modest increase in the film thickness outside of the spots to 8.97 nm.

After further increasing the O_3 pressure to 5 torr, a spot of concentrated deposition was observed (see Figure 6b). A film thickness of 33.58 nm was measured within this concentrated spot, which is significantly higher than the expected 16.80 nm; the thickness outside of this spot was measured to be 8.46 nm. This excessive growth was theorized to be the result of CVD, meaning that the O_3 and $CoCp_2$ were interacting in the gas phase; however, increasing the purge time to 15 s did not change the result seen in Figure 6b.

This lack of improvement after increasing the purge time could be explained by the condensation of $CoCp_2$ within the delivery lines to the reactor. Although $CoCp_2$ sublimates at 40 °C and 0.1 torr, its melting point is only reached at 173-174 °C.³⁷ As the delivery lines were at 150 °C, it could be possible that condensed $CoCp_2$ was collecting within the delivery lines and slowly evaporating over time even while the $CoCp_2$ valve was closed, leading to parasitic CVD. To test this possibility, the temperature of the $CoCp_2$ valve was increased from 150 °C to 180 °C and the temperature of the Co_3O_4 delivery line was increased from 150 °C to 190 °C. A thickness map of this film is presented in Figure 7a. To generate the thickness map, VASE measurements were taken at the white points and film thickness was interpolated between measurements. This change removed the visible showerhead pattern, although a faint dark spot was still visible on the deposited film. The film thickness in the spot was found to be 15.08 nm, meaning that CVD was no longer occurring, but film thickness dropped off steeply, with the remainder of the film only being 0.45 nm thick.

Because the film thickness in Figure 7a was still lower than the expected 16.80 nm,



(a) Film thickness ranges from 0.45 nm to 15.08 nm. (b) Film thickness ranges from 0.32 nm to 16.48 nm. (c) Film thickness ranges from 2.14 nm to 16.01 nm.

Figure 7: Thickness maps of Co_3O_4 films grown with 336 cycles of 1s/10s/10s/10s ($\text{CoCp}_2/\text{N}_2/\text{O}_3/\text{N}_2$), and the substrate heater at 271 °C. In Figure 7a, the temperature of the CoCp_2 delivery line and valve were increased to eliminate CoCp_2 condensation. In Figure 7b, the N_2 flowrate in the CoCp_2 source line was increased from 50 to 75 sccm. In Figure 7c, O_3 pressure was increased from 5 to 10 torr.

and because the precursor could not saturate the entire wafer, lack of precursor was still suspected. To remedy this, the N_2 flowrate in the CoCp_2 delivery lines was increased from 50 to 75 sccm in order to further spread CoCp_2 out within the reactor. This film is shown in Figure 7b, which illustrates a mild improvement in the size of the deposited area. However, the film in Figure 7b still appeared deficient in precursor, so CoCp_2 pulse time was first increased to 1.5 s and then to 3 s to test lack of CoCp_2 . However, when CoCp_2 pulse time was increased, a significant difference from Figure 7b was not observed, except for the presence of CVD in the 3 s CoCp_2 pulse film, ruling out CoCp_2 as the limiting precursor.

Because CoCp_2 was ruled out as the cause of the lack of growth, its pulse time was returned to 1 s and O_3 pressure was instead increased to 10 torr, leading to the film shown in Figure 7c. A significant improvement in uniformity was observed relative to any of the previous films. However, the non-uniformity observed in the film shown in Figure 7c was still 35.56 %, significantly higher than the 4.7 % achieved by Holden and Conley. To further reduce non-uniformity, it was clear that the amount of O_3 in the reactor needed to be increased.

It is known that in certain ALD processes, O_3 undergoes significant surface loss, meaning that O_3 is catalytically decomposed to O_2 by the metal oxide it is trying to grow, necessitating

large amounts of O_3 to grow an ALD film.^{38,39} Co_3O_4 was identified as a high-loss oxide by Knoops et. al., as it required a high O_3 pulse time to uniformly grow.³⁸ It was noted that within the KJL ALD reactor, the substrate was not the first surface where precursor gases were allowed to come into contact; rather, the precursor gases first came into contact with the showerhead above the substrate. Staining indicative of deposition was also noted on the showerhead. Therefore, it was suspected that Co_3O_4 had deposited on the back side of the showerhead and was catalytically degrading O_3 above the showerhead before it could oxidize the surface of the substrate below the showerhead.

To remedy this, the showerhead was removed from the KJL ALD system, leading to the film shown in Figure 8. The removal of the showerhead had a dramatic effect on the overall quality of the film. Visually, the film appeared entirely uniform, and there was no longer a visible dark spot as observed in Figure 6b. The non-uniformity of the film in Figure 8 was also significantly reduced to 4.36 %.

The spot in the middle of Figure 8 only became apparent through VASE measurements and corresponds to where the precursor gases enter the reactor. As the thickness within the spot was 18.63 nm, larger than the expected 16.80 nm, CVD was suspected and purge times were increased to 15 s. However, the lengthened purge time had no effect, so it was returned to 10 s. As any possibility of CVD had been eliminated through the previous set of process adjustments, it was more likely that a GPC higher than $0.05 \frac{nm}{cycle}$

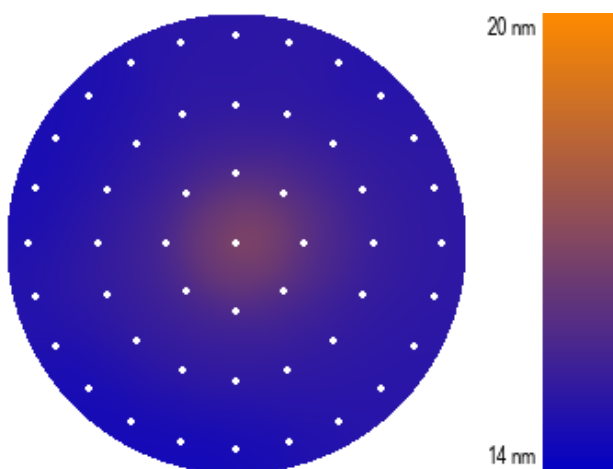


Figure 8: Thickness map of a Co_3O_4 film grown without the showerhead with 336 cycles of 1s/10s/10s/10s ($CoCp_2/N_2/O_3/N_2$) with an O_3 pressure of 10 torr, N_2 flowrate of 50 sccm in the O_3 source line and N_2 flowrate of 75 sccm in the $CoCp_2$ source line, and the substrate heater at 271 °C. The film thickness ranges from 14.35 nm to 18.63 nm. Note that the scale has been adjusted for this thickness map compared to Figures 7a-7c to highlight its non-uniformity.

was being observed. Therefore, limited growth due to lack of precursor was still the most likely explanation for the non-uniformity.

To ensure CoCp₂ was not the limiting precursor, its pulse time was increased to 1.5 s, which had a minimal effect on the film. O₃ pulse time was increased from 10 s to 15 s and then to 30 s, which grew the spot in the middle significantly. However, 30 s O₃ pulses were impractical, as they increased the cycle time significantly. As 10 torr was the maximum the KJL ALD metering valve could achieve, the deposition temperature was decreased from 271 °C to 200 °C to reduce the deactivation rate and therefore prevalence of O₃ surface loss.

The thickness map of the 200 °C deposited film in Figure 9 displays a spot that is much less prevalent than the one in Figure 8. The thickness in this spot was 16.85 nm, close to the expected 16.80 nm. The non-uniformity of this film was found to be 3.08 %, lower than the 4.7 % reported by Holden and Conley.

The high uniformity of the final film can be explained by a lower deposition temperature and high O₃ usage. This suggests that the upper bound of the ALD window for growing Co₃O₄ using CoCp₂ and O₃ is lower than previously reported. This also suggests that O₃ surface loss is significant, requiring further study into its mitigation. Additionally, this film matches the 0.05 $\frac{nm}{cycle}$ GPC found by Holden and Conley, confirming its accuracy. While the film quality could be improved, a film that is more uniform than has been previously reported is a good starting point for analyzing other important properties of electrocatalysts - their stoichiometry and crystalline structure.

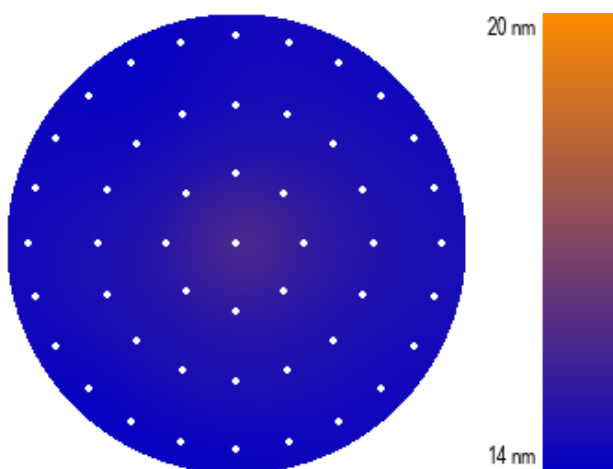


Figure 9: Thickness map of a Co₃O₄ film grown without the showerhead with 336 cycles of 1s/10s/10s/10s (CoCp₂/N₂/O₃/N₂) with an O₃ pressure of 10 torr, N₂ flowrate of 50 sccm in the O₃ source line, N₂ flowrate of 75 sccm in the CoCp₂ source line, and the substrate heater at 200 °C. The film thickness ranges from 14.04 nm to 16.85 nm.

5 Annealing and Characterization

After ALD optimization, Co₃O₄ thin films were annealed to study how film thickness and annealing process parameters affect the crystallinity and stoichiometry of the films. Film thicknesses, annealing temperatures, and gases used during annealing were all varied. The thin films were studied using X-ray photoelectron spectroscopy (XPS) and X-ray diffraction (XRD) both before and after annealing.

5.1 Experimental Methods

A tube furnace with available 10% H₂ and 90% Ar, N₂ and air was used to anneal the films. The tube furnace was heated from room temperature at a rate of 50 $\frac{^{\circ}\text{C}}{\text{min}}$ to the annealing temperature, where it was held for one hour and then allowed to naturally cool to room temperature. All gases were flowed through the furnace at 0.4 sccm.

XPS spectra were captured by a PHI 5000 VersaProbe III Photoelectron Spectrometer. The sample was treated as non-conductive and was placed on an insulating layer during analysis. A 25 W, 100 μm X-ray beam was used to excite photoelectrons. Survey spectra were taken with a step of 1 eV over 6 sweeps. C1s spectra were taken with a step of 0.1 eV over 18 sweeps. O1s spectra were taken with a step of 0.1 eV over 12 sweeps. Co2p spectra were taken with a step of 0.1 eV over 30 sweeps.

XRD spectra were collected by a Bruker D8 Discover X-ray diffractometer. Two frames were collected by an area detector at 45° and 65° with respect to the sample surface normal, with each frame having an exposure time of 30 minutes and a width of 30°. The resulting spectra from both frames were analyzed and stitched together using MDI Jade.

Both 7 nm and 27 nm thick films were tested under N₂, air, and H₂, and at 300 and 600 °C. All films were annealed for 1 hour.

5.2 Results

The 27 nm films were found to be much more crystalline than the 7 nm films before annealing. In Figure 10, the 27 nm film shows a clear (311) peak, while the 7 nm film does not show any of the expected Co_3O_4 peaks. This effect of film thickness was also found to persist after annealing. The annealing procedures tested in this study did not have a significant effect on the 7 nm films, while they had a noticeable one on the 27 nm films. This can be seen when comparing 7 nm films annealed both under air and N_2 (Figures 11a and 11b); there is no apparent difference between 7 nm films that were annealed and 7 nm films that were not annealed. On the other hand, annealing had a noticeable effect on the crystallinity of 27 nm films under N_2 and air.

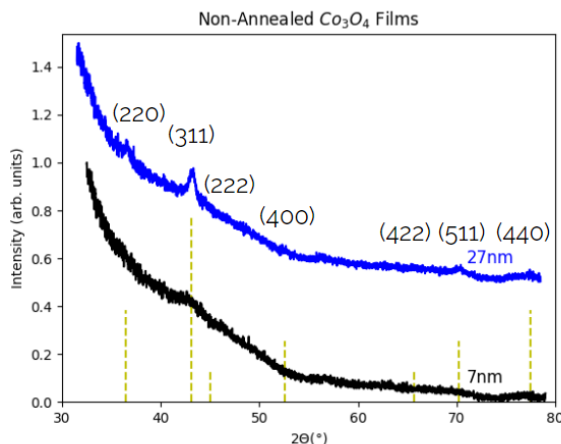


Figure 10: XRD spectra of the 7 nm film and 27 nm film before annealing. The dashed yellow lines show expected peak intensities and 2θ values that correspond to spinel Co_3O_4 .

In Figure 11c, annealing at 300 °C under air did not significantly improve the crystallinity of the 27 nm film, but annealing at 600 °C under air increased the height of the (311) peak and also allowed small (220) and (400) peaks to intensify above the background. In Figure 11d, annealing at 300 °C under N_2 only slightly increased the height of the (311) peak. However, annealing under 600 °C dramatically changed the crystal structure of the cobalt oxide, adding a peak that does not correspond to spinel Co_3O_4 , but rather the (002) plane of halite CoO , indicating that the film was reduced during annealing. This is further confirmed by examining the $\text{Co}2p$ XPS spectrum for the 27 nm film annealed at 600 °C under N_2 (Figure 12a).

Comparing the XPS data from Figure 12a and the shape of the curves from Figure 12c, it

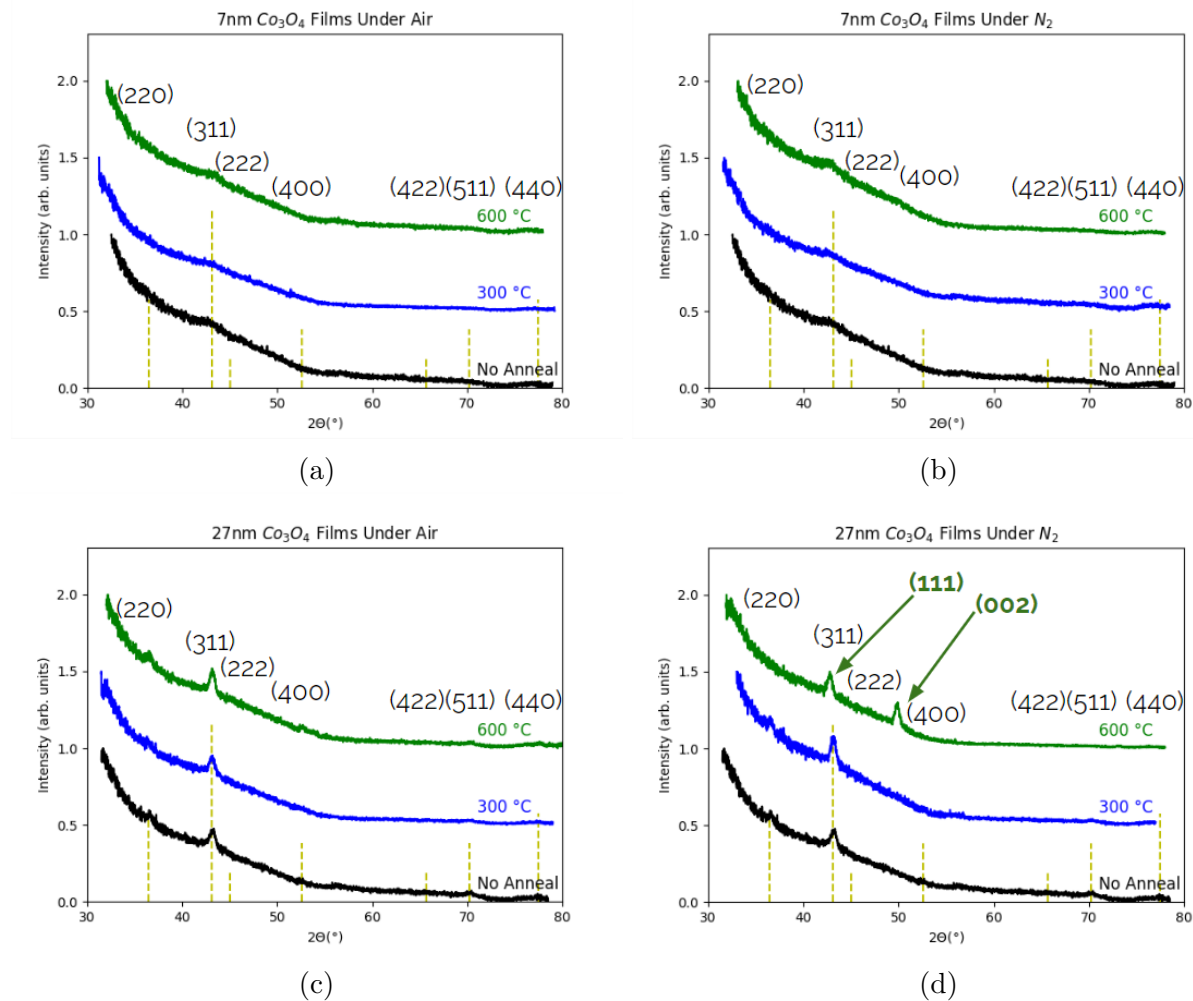


Figure 11: XRD spectra of both 7 and 27 nm films annealed under both air and N_2 . The dashed yellow lines represent expected peak locations and intensities for spinel Co_3O_4 . (a) 7 nm films annealed under air. (b) 7 nm films annealed under N_2 . (c) 27 nm films annealed under air. (d) 27 nm films annealed under N_2 . For the film annealed at 600°C , a reduction to halite CoO was observed, indicated by the appearance of a peak corresponding to the (002) plane of halite CoO . What appears to be a spinel (311) peak is actually from the (111) plane of halite CoO .

is clear that the film has CoO stoichiometry rather than Co_3O_4 stoichiometry. Reduction to CoO was also observed in all of the films annealed in H_2 (see Figure 12b). This is consistent with H_2 being well-known as a reducing agent; however, the effect for N_2 could be explained by the low concentration of O_2 in the gas, which at high temperature created a large difference in the chemical potential of oxygen between Co_3O_4 and the gas, leading to the reduction of the film to CoO .

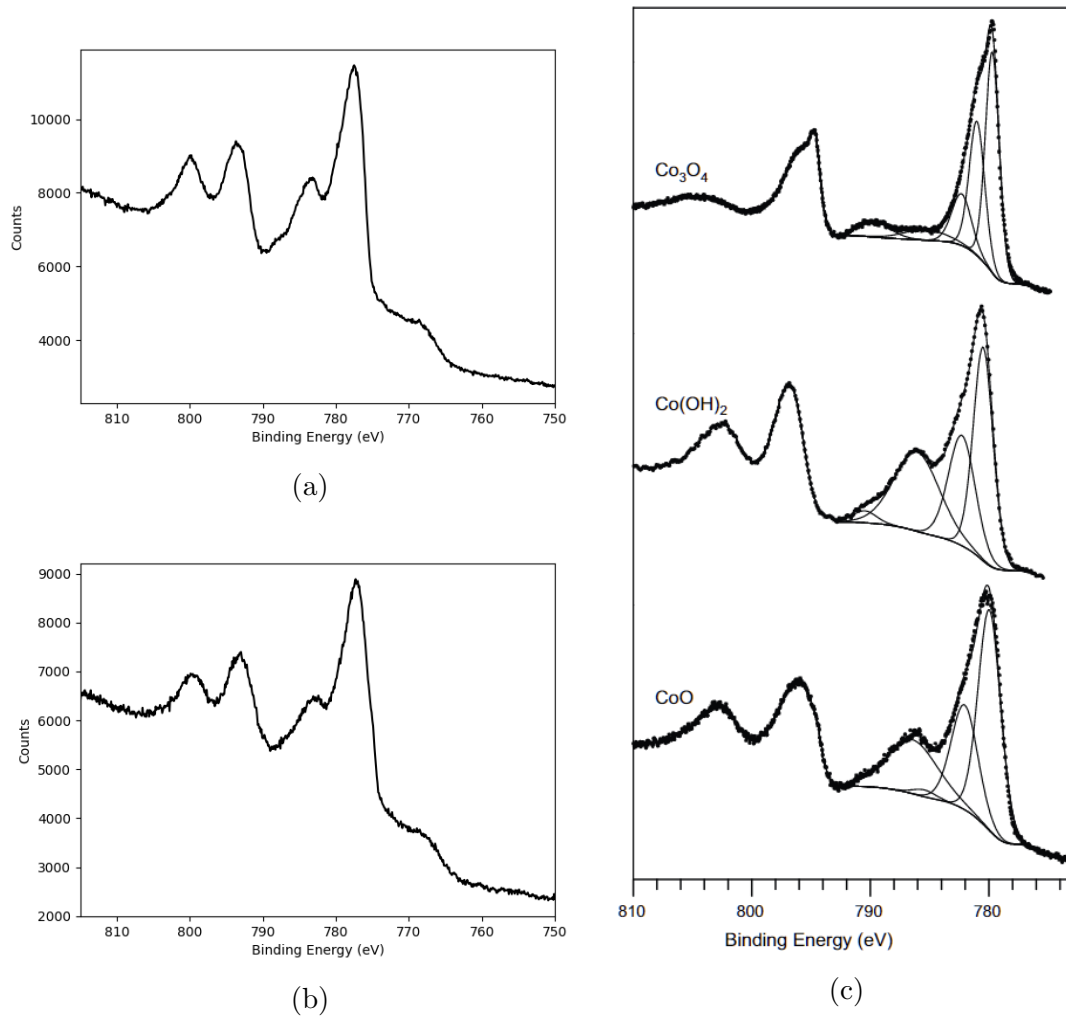


Figure 12: XPS spectra of select reduced films. (a) Co₂p XPS spectrum of a 27 nm cobalt oxide film annealed under N₂ at 600 °C. This spectrum most closely matches the CoO spectrum from Figure 12c. (b) Co₂p XPS spectrum of a 7 nm cobalt oxide film annealed under H₂ at 300 °C. This spectrum most closely matches the CoO spectrum from Figure 12c. (c) Comparison of Co₂p XPS spectra of various cobalt oxide stoichiometries. Adapted from Biesinger et. al.⁴⁰

With regards to stoichiometry, there were no differences found between any of the 7 nm and 27 nm films both before and after annealing. This means that what appears to be a small increase in the (311) peak in the 7 nm film annealed under N₂ at 600 °C (see Figure 11b) is actually from the (111) plane of halite CoO.

6 Conclusions

Thin films of Co_3O_4 were successfully grown via ALD using CoCp_2 and O_3 precursors with a non-uniformity of 3.08 % over a 4" native SiO_2/Si substrate. O_3 surface loss was found to be significant, but was mitigated by using a lower deposition temperature of 200 °C and a 10 s O_3 pulse at 10 torr. There were no differences found between the surface stoichiometries of 7 nm and 27 nm films, both before and after annealing. On the other hand, 27 nm ALD-grown Co_3O_4 films were found to be more crystalline than 7 nm ALD-grown Co_3O_4 films. Additionally, annealing under air improved the crystallinity of 27 nm films but did not affect 7 nm films. Reduction of Co_3O_4 to CoO was observed in cobalt oxide films annealed under a H_2 atmosphere, and at 600 °C under a N_2 atmosphere. Annealing at 600 °C in air improved the crystallinity of 27 nm Co_3O_4 thin films more than annealing at 300 °C.

7 Future Work

More work could be done in increasing the uniformity of the ALD films by further increasing the amount of O_3 in the reactor. Additionally, ALD films with fewer cycles could be grown to study the nucleation behavior of ALD-grown Co_3O_4 . ALD films with more cycles could also be grown to ensure that non-uniformity remains low with large film thicknesses.

Much more work could be done with annealing ALD-grown Co_3O_4 films. As it is known that H_2 and N_2 at high temperatures will reduce the film, the parameter space can be narrowed down to annealing only under air or O_2 . With a narrower parameter space, more annealing temperatures and annealing times can be investigated. There are also many important annealing variables that cannot be meaningfully tested by the current equipment, such as cooling rate, which need to be explored to achieve a full understanding of the Co_3O_4 crystallization process.

8 References

- (1) Fawzy, S.; Osman, A.; Doran, J.; David; Rooney, W. *Environmental Chemistry Letters* **2020**, *18*, 2069–2094.
- (2) Ortiz-Bobea, A.; Ault, T. R.; Carrillo, C. M.; Chambers, R. G.; Lobell, D. B. **2021**, DOI: 10.1038/s41558-021-01000-1.
- (3) Abram, N. J. **2021**, DOI: 10.1038/s43247-020-00065-8.
- (4) Nunez, S.; Arets, E.; Alkemade, R.; Verwer, C.; Leemans, R. *Climatic Change* **2019**, *154*, 351–365.
- (5) BP *Full report – Statistical Review of World Energy 2021*; 2021.
- (6) Li, J.; Dong, S.; Peng, M.; Yang, Z.; Liu, S.; Li, X.; Zhao, C. *Ecological Indicators* **2013**, *34*, 94–102.
- (7) *International Journal of Energy Research* **2019**, *43*, 6078–6107.
- (8) Dorotić, H.; Doračić, B.; Dobravec, V.; Pukšec, T.; Krajačić, G.; Duić, N. *Renewable and Sustainable Energy Reviews* **2019**, *99*, 109–124.
- (9) Amirante, R.; Cassone, E.; Distaso, E.; Tamburrano, P. *Energy Conversion and Management* **2017**, *132*, 372–387.
- (10) Fernandez, C. A.; Hatzell, M. C. *Journal of The Electrochemical Society* **2020**, *167*, 143504.
- (11) Hosseini, S. E.; Wahid, M. A. *Renewable and Sustainable Energy Reviews* **2016**, *57*, 850–866.
- (12) Jiao, Y.; Zheng, Y.; Jaroniec, M.; Qiao, S. Z. *Chemical Society Reviews* **2015**, *44*, 2060–2086.
- (13) Xu, W.; Cao, D.; Moses, O. A.; Sheng, B.; Wu, C.; Shou, H.; Wu, X.; Chen, S.; Song, L. *Nano Research 2021 14:12* **2021**, *14*, 4534–4540.

- (14) Hellstern, T. R.; Benck, J. D.; Kibsgaard, J.; Hahn, C.; Jaramillo, T. F. *Advanced Energy Materials* **2016**, *6*, 1501758.
- (15) Huang, J.; Sheng, H.; Ross, R. D.; Han, J.; Wang, X.; Song, B.; Jin, S. *Nature Communications* **2021**, *12*, 1–11.
- (16) Suen, N. T.; Hung, S. F.; Quan, Q.; Zhang, N.; Xu, Y. J.; Chen, H. M. *Chemical Society Reviews* **2017**, *46*, 337–365.
- (17) Seh, Z. W.; Kibsgaard, J.; Dickens, C. F.; Chorkendorff, I.; Nørskov, J. K.; Jaramillo, T. F. *Science* **2017**, *355*, DOI: 10.1126/science.aad4998.
- (18) Christensen, R.; Hansen, H. A.; Dickens, C. F.; Nørskov, J. K.; Vegge, T. *J. Phys. Chem. C* **2016**, *120*, DOI: 10.1021/acs.jpcc.6b09141.
- (19) Liu, Q.; Chen, Z.; Yan, Z.; Wang, Y.; Wang, E.; Wang, S.; Wang, S.; Sun, G. *ChemElectroChem* **2018**, 1080–1086.
- (20) Béjar, J.; Álvarez-Contreras, L.; Ledesma-García, J.; Arjona, N.; Arriaga, L. G. **2019**, DOI: 10.1016/j.jelechem.2019.113190.
- (21) Tran-Phu, T.; Daiyan, R.; Leverett, J.; Fusco, Z.; Tadich, A.; Bernardo, I. D.; Kiy, A.; Truong, T. N.; Zhang, Q.; Chen, H.; Kluth, P.; Amal, R.; Tricoli, A. *Chemical Engineering Journal* **2022**, *429*, 132180.
- (22) Shanbhag, P. N.; Biswas, R. K.; Pati, S. K.; Sundaresan, A.; Nagesa, C.; Rao, R. **2020**, DOI: 10.1021/acsomega.0c03397.
- (23) Chen, J.; Wu, X.; Selloni, A. *PHYSICAL REVIEW B* **2011**, *83*, 245204.
- (24) Wang, H. Y.; Hung, S. F.; Chen, H. Y.; Chan, T. S.; Chen, H. M.; Liu, B. *Journal of the American Chemical Society* **2016**, *138*, 36–39.
- (25) Xu, Y.; Zhang, F.; Sheng, T.; Ye, T.; Yi, D.; Yang, Y.; Liu, S.; Wang, X.; Yao, J. *Journal of Materials Chemistry A* **2019**, *7*, 23191–23198.

- (26) Wang, Y.; Zhou, T.; Jiang, K.; Da, P.; Peng, Z.; Tang, J.; Kong, B.; Cai, W. B.; Yang, Z.; Zheng, G. *Advanced Energy Materials* **2014**, *4*, 1400696.
- (27) Hu, Z.; ab Liping Hao; ab, F. Q.; Guo, R. *Cite this: Catal. Sci. Technol* **2022**, *12*, 436.
- (28) Li, Z.; Yu, X. Y.; Paik, U. *Journal of Power Sources* **2016**, *310*, 41–46.
- (29) Xiao, Z.; Wang, Y.; Huang, Y. C.; Wei, Z.; Dong, C. L.; Ma, J.; Shen, S.; Li, Y.; Wang, S. *Energy & Environmental Science* **2017**, *10*, 2563–2569.
- (30) Liu, X.; Liu, H.; He, G.; Zhu, Y.; Xiao, J.; Han, L. *Catalysts 2021, Vol. 11, Page 659* **2021**, *11*, 659.
- (31) Cremers, V.; Puurunen, R. L.; Dendooven, J. *Appl. Phys. Rev* **2019**, *6*, 21302.
- (32) Klepper, K. B.; Nilsen, O.; Fjellvåg, H. *Thin Solid Films* **2007**, *515*, 7772–7781.
- (33) Han, B.; Choi, K. H.; Park, K.; Han, W. S.; Lee, W. J. *Electrochemical and Solid-State Letters* **2012**, *15*, D14.
- (34) Holden, K. E. K.; Conley, J. F. *Journal of Vacuum Science & Technology A* **2019**, *37*, 020903.
- (35) Elers, K.-E.; Blomberg, T.; Peussa, M.; Aitchison, B.; Haukka, S.; Marcus, S. **2006**, DOI: 10.1002/cvde.200500024.
- (36) Vos, M.; Mackus, A.; Kessels, E. *Atomic Layer Deposition Process Development*; 2019.
- (37) COBALTOCENE <https://cameochemicals.noaa.gov/chemical/20042> (accessed 03/24/2022).
- (38) Knoops, H. C. M.; Elam, J. W.; Libera, J. A.; Kessels, W. M. M. *Chem. Mater* **2011**, *23*, 2381–2387.
- (39) Li, W.; Oyama, S. T. *Journal of the American Chemical Society* **1998**, *120*, 9047–9052.

- (40) Biesinger, M. C.; Payne, B. P.; Grosvenor, A. P.; Lau, L. W.; Gerson, A. R.; Smart, R. S. C. *Applied Surface Science* **2011**, *257*, 2717–2730.